LUNAR DUST SIMULANT PARTICLE ADHESION ON COPOLYIMIDE ALKYL ETHERS

Christopher J. Wohl,[1,] Leanna L. Foster,[2] Dawson E. Connell,[2] William T. Kim,[2] Denizhan Yavas,[3] Ashraf Bastawros,[3] and John W. Connell[1]*

[1]NASA Langley Research Center, Hampton, VA 23681
[2]NASA Langley Research Summer Scholars, NASA Langley Research Center, Hampton, VA 23681
[3] Department of Aerospace Engineering, Iowa State University, Ames, IA 50011

christopher.j.wohl@nasa.gov

Abstract

Mitigation of lunar dust contamination is one of the greatest challenges to be overcome to realize a sustained lunar presence. Likely solutions will integrate active mitigation strategies, requiring the input of external energy, and passive materials, exhibiting an intrinsic resistance to lunar dust adhesion. In this work, a series of copolyimide alkyl ethers containing perfluorinated side-chains were generated to evaluate the influence surface modification agents have on surface chemical, topographical, and mechanical properties. An expanded testing protocol to characterize the adhesion interaction between lunar dust simulant and the copolyimide substrate was carried out. The interfacial adhesion strength was in-situ measured by a custom-built particulate adhesion instrument, utilizing a sonic wand. Surface mechanical properties were characterized by nanoindentation, utilizing the continuous stiffness measurement approach. A nominal presence of surface modifying agents, 1 wt%, resulted in a six-fold reduction in adhesion strength of the interface. A strong inverse correlation between the adhesion strength and Young's modulus of the substrate was identified. The reduction was attributed to a synergistic interaction between the surface energy, surface roughness, and modulus of the copolyimide alkyl ethers film.

Keywords

Lunar Dust, Particulate Adhesion, Surface Migration, Oxetane, Fluorinated Surface, Nano Indentation, Nano-asperity Contact

Introduction

Extra-terrestrial exploration has been an active area of scientific research ever since it was discovered by Babylonian astronomers that planets other than Earth existed. Thus, it is no surprise that a significant number of NASA's missions have, historically, been focused on understanding more about other planets in our solar system and, with recent advances in their detection, planets that orbit other stars. However, one of the major challenges regarding mission success in these endeavors has long been identification and application of materials capable of surviving in these extreme environments. Satellites in low Earth orbit (LEO) are constantly bombarded by atomic oxygen (Banks et al., 2004) and those travelling through interplanetary space face challenging levels of radiation (Chancellor et al., 2018, Goswami et al., 2012, Simonsen et al., 2000). Although significant research efforts have identified atomic-oxygen resistant materials (Connell, 2000) and radiation protecting systems (Thibeault et al., 2015), these extreme environment hazards still present a formidable challenge.

For extra-terrestrial surface missions, there are a gamut of extreme environments that impede research activities. One of the most difficult hazards to mitigate, as identified in the 2013 Global Exploration Roadmap, is particulates or dust (ISECG, 2013). This was certainly demonstrated during the Apollo missions as the lunar dust infiltrated all exposed surfaces clogging gears, compromising seals, abrading visors and gloves, and potentially presenting health hazards to the crew (Gaier, 2005, Gaier et al., 2010). Difficulties with particulate contamination were also experienced on the Martian surface as dust accumulation reduced the efficiency of solar energy harvesting which was partially restored by a serendipitous dust devil (Lorenz et al., 2015). A decline in performance of lunar retroreflectors left by the Apollo XIV astronauts has also been attributed to the continual accumulation of lunar dust on the

reflective surfaces arising from peculiar dust levitation and migration processes (Murphy Jr. et al., 2010).

Numerous methodologies have been developed to mitigate extraterrestrial dust contamination, which can be readily separated into two categories, active and passive approaches (Afshar-Mohajer et al., 2015). Active mitigation strategies are those that require input from an external energy source such as electrostatic dust screens (Calle et al., 2008, Horenstein et al., 2013) and regolith microwave sintering devices (Lim et al., 2017, Lim et al., 2019). Passive mitigation strategies require no external energy as the dust mitigation properties are intrinsic to the material. Most materials developed as passive dust adhesion mitigation surfaces have been biomimetic, imitating solutions found in natural systems, such as the self-cleaning properties of many leaf surfaces (Barthlott et al., 1997, Wong et al., 2011). Although most natural systems require water for self-cleaning, which is not present in the liquid form in either lunar or Martian environments, the principles taken from these terrestrial examples are still considered to be relevant in dry, extraterrestrial locations. The success of self-cleaning plants arises from two main surface properties, hierarchical surface topographies and low surface energy chemical functionalities (Nosonovsky et al., 2007, Celia et al., 2013, Quere, 2008). Using these observations, researchers have fabricated a multitude of biomimetic, self-cleaning, superhydrophobic surfaces (Kesong et al., 2012, Nishimoto et al., 2013, Geim et al., 2003, Jung et al., 2011).

Lunar dust will present a unique challenge regarding the need to mitigate or minimize its influence on long duration mission success (Figure 1, Walton, 2007, Calle, 2017, Eberhard et al., 2011, Heiken, et al., 1991). Extra-terrestrial habitation has received renewed interest, especially with the identification of water deposits on both the lunar and Martian surfaces (Liu et al., 2012, Shuai et al., 2018, Carr et al., 2015). The specific lunar dust particle size range of interest for this work consists of particulates with diameters ≤ 50 μm. These particles have largely been generated through meteorite and micrometeorite impacts (Popel et al., 2018, Popel et al., 2020). As a result, many of the particles consists of agglutinated smaller particles, often forming complex, jagged conformations. The energy from impacts can result in formation of glassy deposits and elemental iron patinas (McKay et al., 2014). Lunar dust particle

surfaces can also be chemically reactive due to the lack of an atmosphere. Finally, dust particles have been observed to levitate and translate across the lunar surface due to unique and complex electron transport phenomena between the day and night sides of the Moon (Horanyi et al., 2015, Stubbs et al., 2006, Abbas et al., 2007). This dust levitation was observed as a horizon glow at the lunar terminator (the day-night line) when viewed from the far side of the Moon. Collectively, these particulate properties and environmental conditions make identification of materials that would exhibit intrinsic lunar dust adhesion mitigation properties challenging.

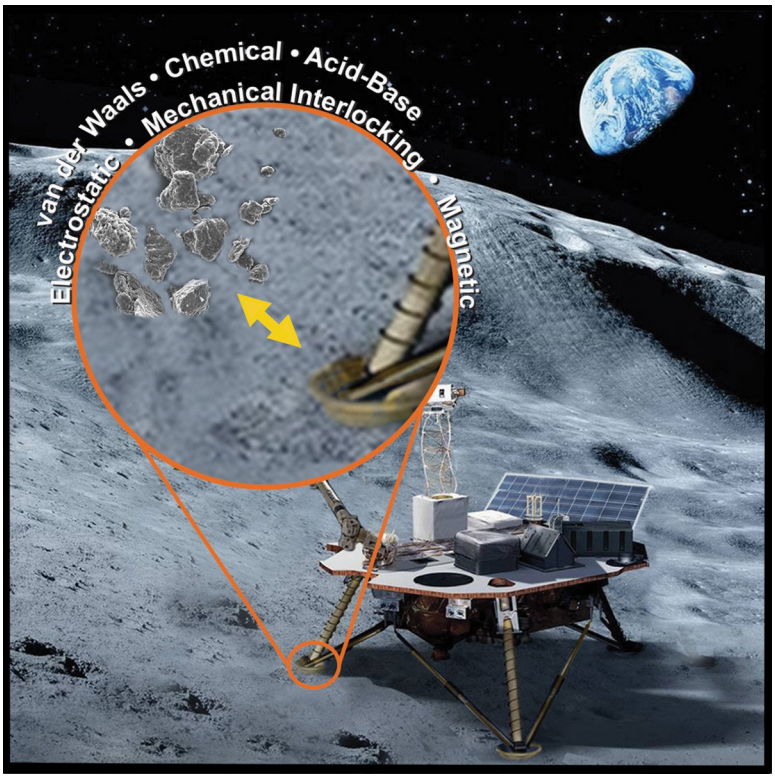

Figure 1. Lunar dust will interact with exposed surfaces through a myriad of mechanisms. *Image credit: Susanne Waltz, Media Fusion.*

Surface modification has become a broadly utilized technique to impart changes in the response of a surface to an environmental stimulus with the benefit of largely retaining bulk properties (Pinson et al., 2019). There are a number of techniques for modification of existing polymeric surfaces; plasma, laser ablation, corona discharge, etc. Surface modifying agents, though, are an approach to controllably alter a polymeric material's surface properties as it is being prepared (Zhang et al., 2019, Harney et al., 2009, Sangermano et al., 2003). These moieties will typically possess either silicone (Si) or fluorine (F)

functionalities. Thermodynamically, the surface modifying agent experiences less favorable interactions with the surrounding polymer matrix than at the polymer-air interface. These moieties will migrate to the surface to populate a more enthalpically favorable environment overcoming the entropic cost of surface concentration. The resultant polymeric material will exhibit surface chemical and mechanical properties that can deviate significantly from the bulk properties. Teflon-like surfaces have been demonstrated in partially fluorinated matrices using this approach (Tan et al., 2004, Glaris et al., 2015).

In this work, a series of copolyimide materials were evaluated for use as lunar dust adhesion mitigating materials via a custom-built particulate adhesion instrument. Differences in alkyl ether structure resulted in changes to surface mechanical properties manifesting as strong differences in adhesion force, amounting to six-fold differences. These differences are reconciled through measurements of the surface roughness, adhesion energy and mechanical properties of the surface modified copolyimide material system. Details of the experimental protocol, experimental results and analysis are elaborated.

Experimental

Materials and Methods. The copolyimide alkyl ethers utilized in this work were synthesized as described previously (Scheme 1, Wohl et al., 2015). In short, a series of amine-terminated alkyl ethers were synthesized through a two-step reaction starting with hydroxyl-terminated partially fluorinated oxetane-derived alkyl ethers (PolyFox materials, Omnova Solutions, Beachwood, OH). These surface modifying oligomers were combined with an aromatic dianhydride (3,3',4,4'-biphenyl tetracarboxylic dianhydride, s-BPDA, ChrisKev Company) and an aromatic diamine (4,4'-oxydianiline, 4,4-ODA, Wakayama Seika Kogya) forming a polyamide acid intermediate. The total surface modifying oligomer content was 1 wt% for each oligomer utilized in this work. Film-casting these solutions followed by thermal imidization, liberating the water byproduct and generating the permanent imide heterocycle,

yielded free-standing copolyimide alkyl ether films. The compositions utilized in this work are described in Table 1.

Scheme 1. Copolyimide alkyl ether synthesis.

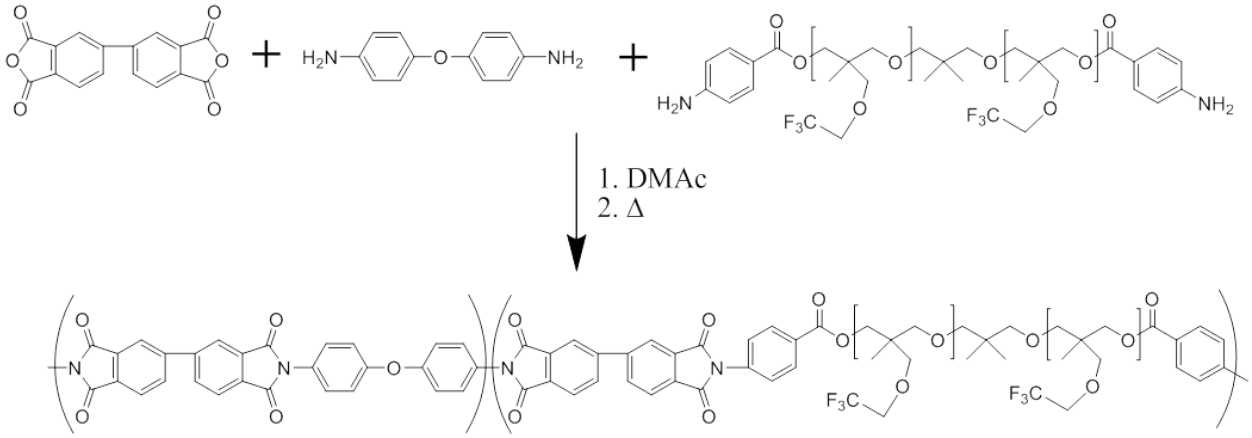

Table 1. Copolyimide alkyl ether compositions. All compositions included s-BPDA, 4,4'-ODA, and 1 wt% of the alkyl ether.

	Polyfox	Oligomer Molecular Weight	Number of F Atoms per Oligomer	Tensile Modulus, MPa	θ_A
PI Control	--	--	--	3590±110	80±2
$PIAEF_{18}$	PF636	1310	18	3230±50	108±4
$PIAEF_{30}$	PF656	1530	30	3190±110	94±4
$PIAEF_{30B}$	PF154N	3200	30	3010±60	95±2
$PIAEF_{40}$	PF7002	1640	40	3510±70	98±2
$PIAEF_{60}$	PF6320	4740	60	3440±70	91±2

Lunar Dust Simulant Adhesion Determination. Adhesion experiments were conducted utilizing NASA/USGS Lunar Highlands Simulant with particle diameters ≤ 25 μm. Figure 2 shows a scanning electron microscopy (SEM) micrograph of the simulant with the rough surfaces and angularity described in actual lunar dust. The adhesion-testing apparatus (Figure 3) was previously described in detail (Wohl, 2011). It consisted of an aluminum environmental chamber (Abbess Instruments and Systems Inc., Holliston, MA, 0.227 m^3), a 20 kHz sonication device (Vibracell VCX-750, Sonics and Materials Inc., Newtown, CT), and an optical particle counter (Solair 3100, Lighthouse Worldwide

Solutions, San Jose, CA). All measurements were conducted at ambient pressure within the environmental chamber. Samples were prepared by affixing a 6 mm circle of the substrate, cut from a hole punch, onto the tip of the sonication device (12.7 mm diameter) using a cyano-acrylate adhesive (Hot Stuff, Satellite City Inc., Simi, CA). It should be noted that the dynamics of the developed adhesion-testing apparatus are unique in directly applying the forces normal to the adhesion surface, and thereby it can be accurately correlated to the adhesion forces and adhesion energy. This is different from the commonly utilized centrifugal system, wherein the centripetal decohesion force is applied to shear off the particle from the surface, in a sliding or a rolling motion (Wang, 1990). In this type of system, the cohesion forces might be very different when measured in shear mode vs. tensile mode due to asperity interaction at the interface (Evans and Hutchinson, 1989).

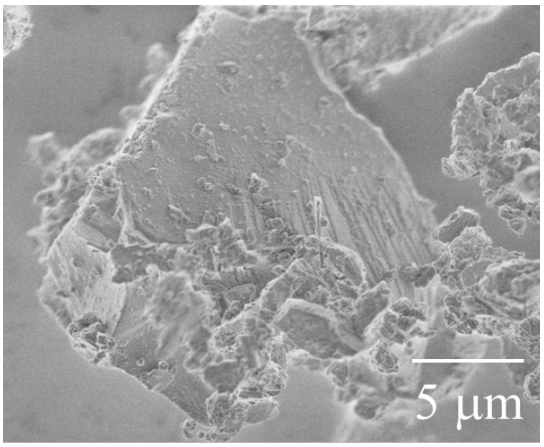

Figure 2. SEM micrograph of rough surface topology present in lunar dust simulant.

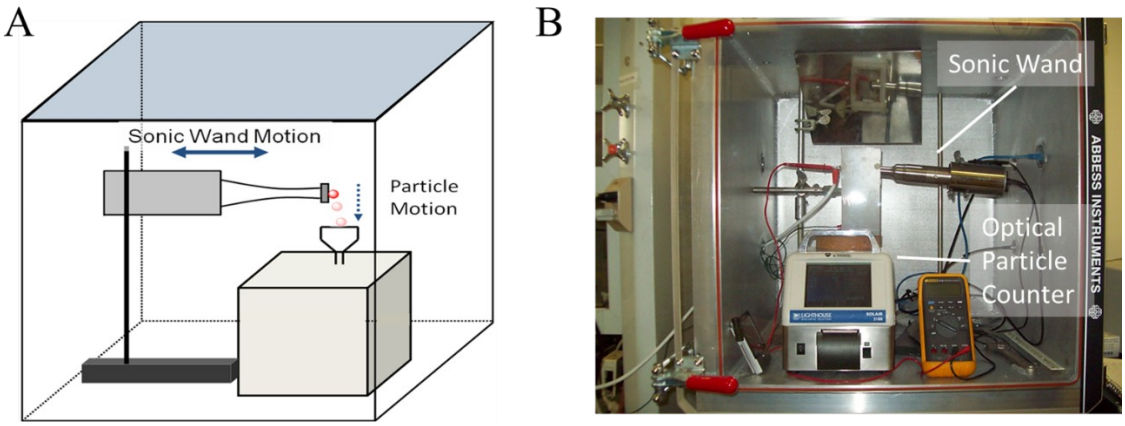

Figure 3. An illustration (A) and an image (B) of the particulate adhesion-testing device.

In order to yield accurate and reproducible adhesion data, an approximate monolayer coating of particulate material was necessary. To achieve an approximate monolayer coating, a simple aerosolization technique was developed where particulates were lofted into the free space of an enclosed container, kept at ambient conditions, using approximately one burst per milligram of particles from a compressed air canister (Figure 4). Optical microscopy was used to verify the extent of particulate coating. Particulate coating was restricted to the area comparable to the hole punch size and particulates deposited outside this region were carefully removed using dust free laboratory wipes (Kimwipe®, Kimtech Sciences). Pre-sonication micrographs were taken documenting particulates deposited on the substrate and particulates remaining at the completion of the simulant detachment experiment, respectively, as depicted in Figure 5.

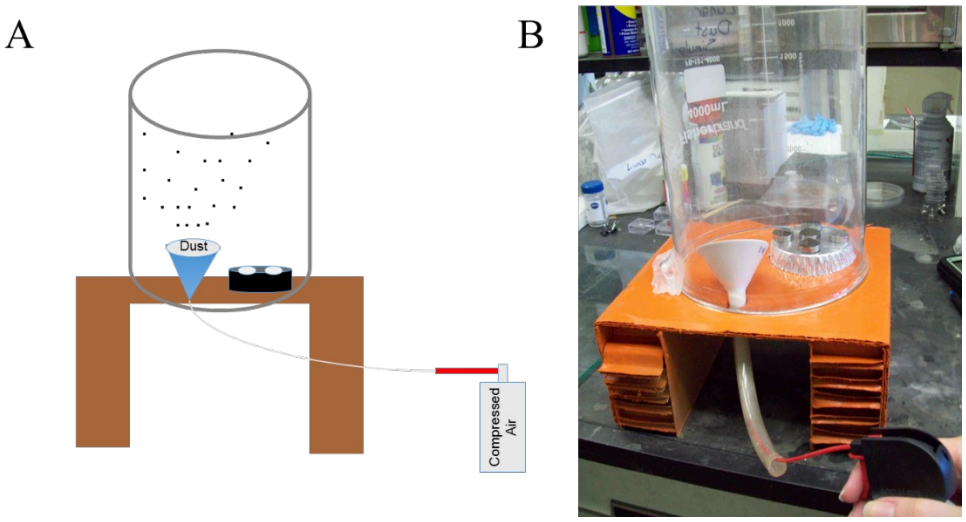

Figure 4. An illustration (A) and an image (B) of the particulate contamination chamber.

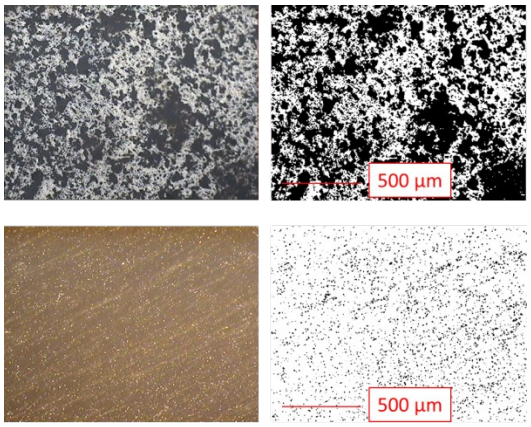

Figure 5. Pre-sonication (top) and post-sonication (bottom) images of a copolyimide alkyl ether surface with lunar simulant deposits. The images on the left are the optical micrographs and the images on the right are the same images after Image J analysis.

Particle detachment experiments were conducted by applying a programmed series of sonic wand pulses synchronized with the optical particle counter via a LabVIEW virtual instrument program. To enable collection, fitting, and removal of background contribution to the detected particles, a period of 15 s prior to, and at the completion of the sonic wand activity was utilized to collect ambient particle counts. Ambient aerosolized particles in the range of interest, 10-25 μm, were observed to decay at an exponential rate. This suggested some level of turbulence was created in the closed environment by the exhaust from the optical particle counter (Bosse et al., 2006), though this was not anticipated to alter the results from the particle detachment studies. Starting at the minimum displacement amplitude of 25 μm (~20%), the displacement amplitude was increased in 2% increments up to the maximum displacement of 124 μm (100%). The sonic wand was activated four times for 0.5 s at each displacement amplitude with a 7 s break between pulses to enable the optical particle counter values to return to ambient levels. Once completed, the collected particle count data was sorted into sonic wand active and inactive data points. The sonic wand inactive data points were fitted to an exponential decay function and this was applied as a background subtraction from the sonic wand active data set. This data, along with the

surface clearance percentage ($Clear_{\%}$), described below, was utilized to calculate the force required to remove 50%, by surface area. of the deposited lunar dust simulant particles, $Clear_{50\%}$.

After completion of the particulate detachment experiment, the sample surface was imaged using optical microscopy to determine percent surface clearance, $Clear_{\%}$. For surfaces that exhibited complete clearance, the data from the optical particle counter was used directly. For surfaces that did not completely clear, ImageJ software was used to approximate percent clearance by determining the area of the image coated with particulate material, $Area_0$ and $Area_F$ from the optical images collected before and after the particulate detachment experiment, respectively. To perform the particle analysis, the optical micrograph samples were converted to an 8-bit gray scale image and then converted to a threshold image where the lower and upper threshold limits were set to separate the particulate material from the substrate. Size and circularity patterns were adjusted to capture particle sizes of significance for the particular study. $Clear_{\%}$ was calculated according to:

$$Clear_{\%} = \left(1 - \frac{Area_F}{Area_0}\right) \times 100\,\% \tag{1}$$

The particulate adhesion force was considered to be equal to the detachment force required to observe the particulate with the optical particle counter. This assumes that the substrate mechanical response remains elastic during the particulate release process. Using the particle's size and the kinematics of the vibration motion of the sonic actuator, the detachment force can be determined according to:

$$F_{Detach} = ma \tag{2}$$

where m is the mass of a particle and a, the surface acceleration, is computed from (Zimon, 1969):

$$a = 4\pi^2 f^2 A \tag{3}$$

where f and A denote the frequency and amplitude of oscillation, respectively. This relationship assumes that the change in acceleration of the sonic wand follows a sinusoidal pattern. $Clear_{50\%}$ was calculated by scaling the displacement amplitude, and therefore the F_{Detach} value, to the value at which

50% of the total deposited particulates were detached from the interrogated surface. All reported measurements in this work are for optical particle counter bin of 10 μm. Thus, a 10 μm mean particle diameter will be used in all the analysis.

Nanoindentation Characterization. Nanoindentation was utilized to probe the effective mechanical properties including Young's modulus, E, and hardness, H_c, of different the surface modifying copolyimide alkyl ether fluorinated, PIAEF, films to correlate the substrate mechanical effect on the measured adhesion forces and energies (Doerner et al., 1986, Oliver et al., 1992). Nanoindentation is suitable to probe subtle changes near the film's surface, as well as the progressive changes of properties into the film core (Yang et al., 2009, Yavas et al., 2017a, Yavas et al., 2017b). All indentations were performed in force control using the Hysitron TI 950 TriboIndenter (TriboIndentor™ by Hysitron Inc.). A trapezoidal loading profile, which consisted of a 5 s linear loading, 2 s hold at the peak load, and 5 s linear unload, was utilized to impose regular patterns of nanoindentation using a cube corner tip with a tip radius of about 100-150 nm. Several indentations were performed on each sample with a peak load of 750 μN. Continuous stiffness measurement mode was utilized to measure the variation of the contact modulus and hardness with the depth from the free surface of the modified film. Figure 6 shows a representative set of force and indentation depth curves obtained from indentations preformed on the reference (polyimide with no surface modifying agent), and specimens with a different number of F atoms per oligomer, showing more compliant response.

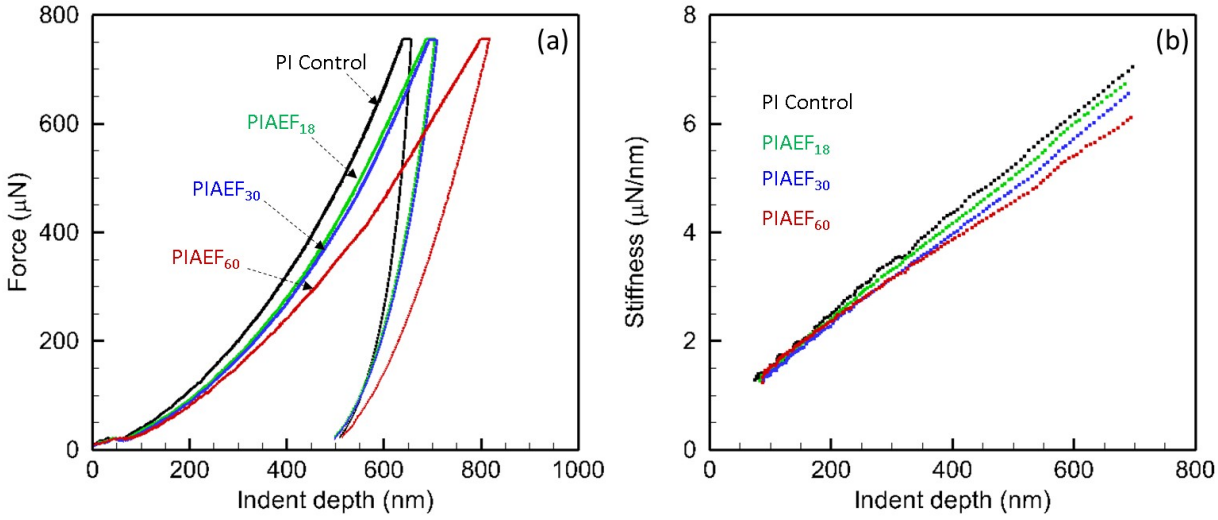

Figure 6. (a) A representative set of force-indent depth curves for the 'Control' and surface modifying agent-containing samples with different number of F-atoms per oligomer. (b) The corresponding variation of the measured contact stiffness as a function of indent depth.

Data analysis method proposed by Oliver and Pharr (1992) was utilized to determine hardness, H_c, and reduced modulus, E_r. H_c was calculated as follows,

$$H_c = \frac{F_{max}}{A} \tag{4}$$

where F_{max} is the maximum load and A_c is the corresponding contact area which is obtained from the indentation depth using the tip-area correlation function, evaluated at every step of the loading increment. In addition, E_r was determined by following expression,

$$E_r = \frac{\sqrt{\pi} S}{2\sqrt{A_c}} \tag{5}$$

where S is the slope of the unloading curve obtained by curve fitting. The indentation-derived Young's modulus, E, after accounting for the indenter tip modulus, E_{tip}, was given by,

$$\frac{1}{E_r} = \frac{1 - \nu^2}{E} + \frac{1 - \nu_{tip}^2}{E_{tip}} \tag{6}$$

Results and Discussion

Lunar dust simulant adhesion testing was performed on a series of copolyimide alkyl ether materials containing different partially fluorinated moieties. This characterization was performed by lightly depositing lunar dust simulant onto surfaces of interest through aerosolization. Once generated, the contaminated specimens were mounted to an ultrasonic device that was subsequently activated at increasing displacements above an optical particle counter. Particles were detected as they fell from the sample surface (Figure 7). Optical particle counter measurements performed while the ultrasonic device was not active were utilized to characterize and subtract the ambient particle population. Optical microscopy was used to determine the initial and final surface contamination levels (Figure 5). Using image analysis, these images were utilized to calculate initial, final and *Clear50%* contaminant surface coverage percentages.

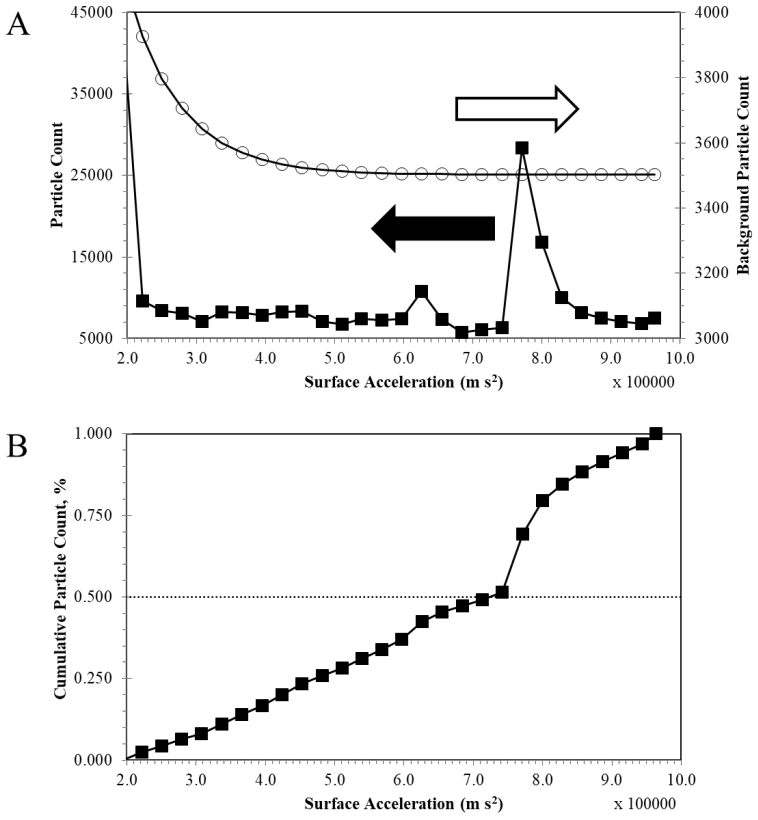

Figure 7. (A) Example of raw data and background data collected during a particle detachment experiment. (B) Cumulative particle count data after background subtraction. The surface acceleration value where the cumulative particle count crosses the dashed line represents the $Clear_{50\%}$ value.

Precise particle deposition control for sample preparation was not possible in this study. However, the generated data was utilized to ascertain consistency throughout the particle detachment experiments. Cumulative particle counts were compared to the calculated number of particles in an ideal monolayer. The number of particles required to form an ideal monolayer on the sample surface, a 6 mm diameter circle, was determined by approximating the lunar simulant as spheres arranged in a face-centered cubic closest packing configuration. A monolayer consisting of only 5 μm or 10 μm particles would contain 283,000 or 71,000 particles, respectively. Calculated cumulative particle counts were typically less than 50% of these values, and often significantly lower. This indicated that, although there may have been aggregated species of few particles at the beginning of each experiment, these aggregates never resulted in particle concentrations greater than what would be present in a monolayer of particles on the surface. With the particle-particle cohesion force (230 nN for 12.5 μm particles) (Oudayer et al., 2018) being comparable or lower than the adhesion force determined on the surfaces evaluated in this work, initially aggregated particles may separate and become adhered to the surface being interrogated immediately after the cohesion force was overcome.

As can be seen below (Table 2 and Figure 8), as the degree of surface modifying oligomer fluorination increased, the overall clearance of lunar dust simulant increased and the *Clear50%* force decreased, exhibiting more than five-fold modulation of the interfacial particle-substrate adhesive force. Interestingly, the mechanical properties as highlighted in Table 1 do not provide a simple relationship between adhesion testing parameters and advancing water contact angle or tensile modulus (collected from a macroscopic tensile test of film segments). This is indicative that confluence of the surface energy, surface morphology and surface mechanical properties may synergistically play a significant role in surface-particle interactions as will be discussed below.

Table 2. Lunar dust simulant adhesion testing results.

	Clear%	Clear50%, μN
PI Control	77%	1.59
$PIAEF_{18}$	73%	1.26
$PIAEF_{30}$	68%	0.69
$PIAEF_{30B}$	93%	0.75
$PIAEF_{40}$	93%	0.80
$PIAEF_{60}$	100%	0.30

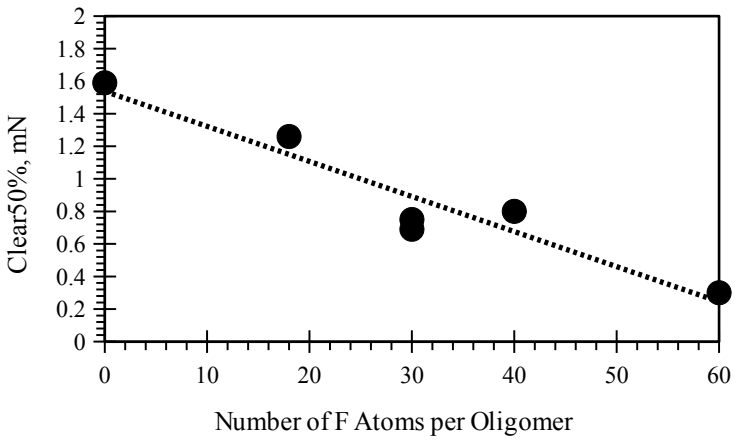

Figure 8. $Clear_{50\%}$ values determined for 10 μm lunar simulant particles on copolyimide alkyl ether surfaces.

The continuous stiffness measurements shed some light on the role of the number of F atoms per oligomer. A summary of the nanoindentation measurements along with the average root mean square (RMS) surface roughness and average dominant roughness wavelength, λ, are summarized in Table 3. Surface properties are the initial surface values at a depth of about 100 nm, the depth where a reliable contact stiffness can be measured. The reported bulk propertied are the average values recorded at a depth of 550 nm, where near plateau values were reached. Figure 9 shows the depth variation of both *E*

and *H* for different copolyimide surfaces. The details were quite subtle, though there was a clear difference in moduli (either the near surface or the bulk moduli) between different copolyimide compositions. The hardness *H* did not show a statistically significant strong correlation, implying that the presence of different surface modifying oligomers did not significantly change the surface hardness, except for $PIAEF_{18}$.

Table 3._Summary of the measured nanoindentation modulus and hardness sampled at the surface (~100 nm) and bulk (~650 nm) of the samples, along with the asperity RMS roughness and the smallest asperity mean spacing, λ, determined by atomic force microscopy, AFM.

	Storage Modulus, GPa (Surface/Bulk)	**Hardness, GPa (Surface/Bulk)**	**RMS Roughness, (nm)**	**λ, (nm)**
PI Control	5.53±0.13/5.56±0.02	~0.73±0.06/0.63±0.01	0.20	900
$PIAEF_{18}$	5.24±0.07/5.39±0.05	~0.95±0.07/0.67±0.01	0.42	875
$PIAEF_{30}$	4.79±0.07/5.08±0.10	~0.64±0.04/0.63±0.01	0.29	285
$PIAEF_{30B}$	4.83±0.22/5.05±0.04	~0.53±0.22/0.62±0.01	0.49	400
$PIAEF_{40}$	5.22±0.20/4.98±0.09	~0.70±0.08/0.64±0.02	0.60	650
$PIAEF_{60}$	5.15±0.12/4.83±0.02	~0.69±0.05/0.64±0.01	1.75	570

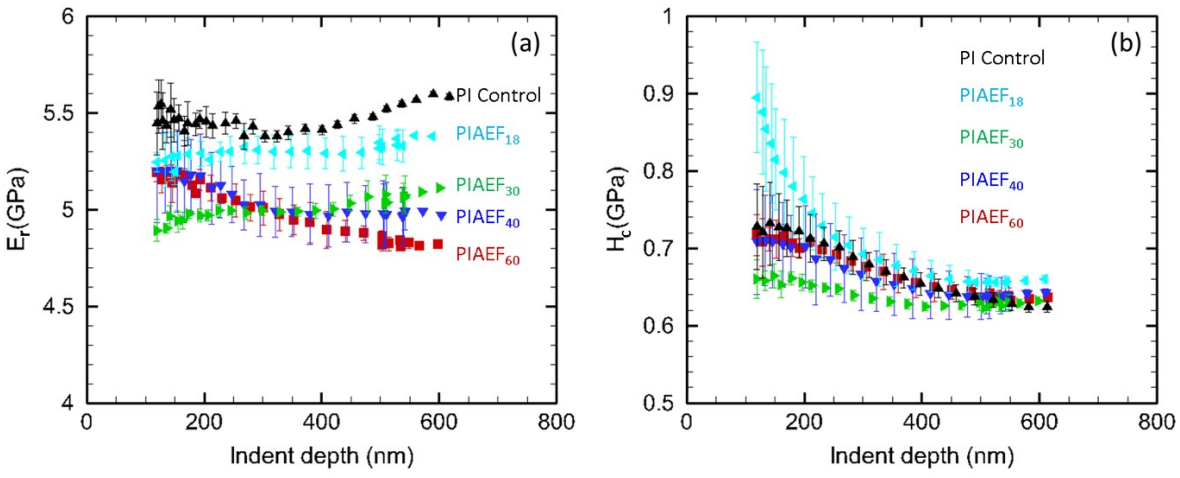

Figure 9. Variation of surface mechanical properties as a function of indent depth for the examined samples; (a) indentation modulus, E_r, and (b) hardness, H_c. The data points are the average of at least three independent measurements and presented with the error bars denoting standard deviation.

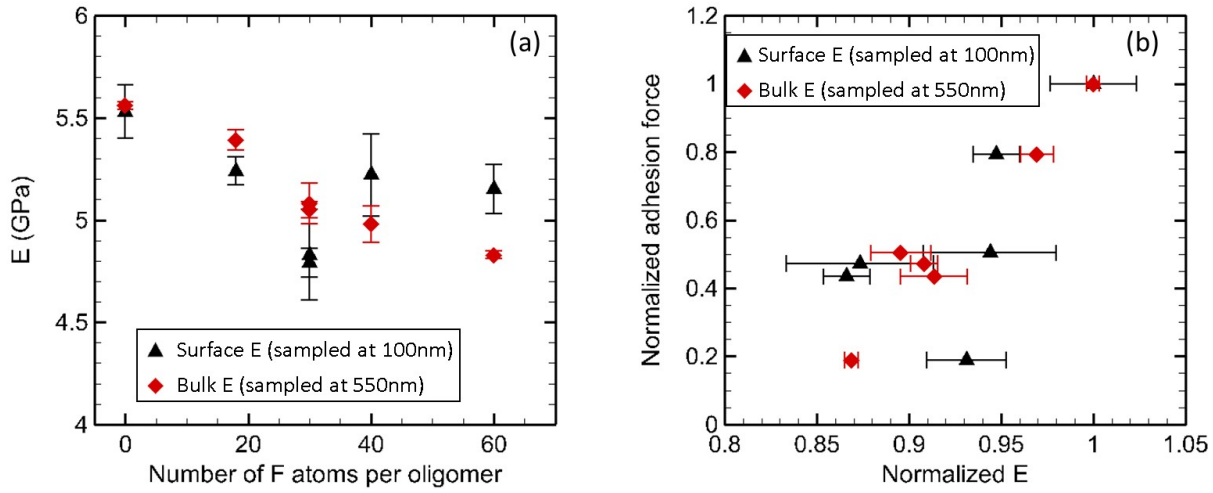

Figure 10. (a) The variation of the surface modulus (sampled at 100 nm) and bulk modulus (sampled at 550 nm) with number of F atoms per oligomer. (b) The variation of the normalized adhesion with the normalized surface modulus (sampled at 100 nm) and bulk modulus (sampled at 550 nm). Control specimen properties were used for normalization.

To highlight the role of the surface modifying oligomer on the indentation modulus, Figure 10(a) summarizes the measured indentation modulus with the number of F atoms per oligomer. A strong decay in indentation modulus was observed, both at the surface and in the bulk of the film. To rationalize the effect of reduction in the modulus on the measured adhesion force, Figure 10(b) summarizes the correlation in a normalized form with the reference sample properties. The experimental measurements show clear proportionality between F_{detach} and E. Though while E dropped by 15%, F_{detach} was modulated by 80%. Another was to understand this disparity is that a change in E by 1.17 corresponds to five-fold reduction in the adhesion force. The observed trend in Figure 10 is unique as (i) the trend is not supported by contact mechanics theories for elasto-plastic bodies with adhesion

(e.g. DMT: Derjaguin, Muller, & Toporov, 1975; and JKR: Johnson, Kendall, & Roberts, 1971), wherein the detachment force does not depend on the surface modulus, and (ii) the trend is reversed compared to the previously reported experimental trend of four-fold increase in adhesion force of 7 μm silica coated particles on a ceramer substrate with a seven-fold reduction in its modulus (Dejesus et al., 2006). In their work, the strong modulation of the adhesion forces were attributed to asperity roughness, without a clear mechanistic view of the role of surface modulus. For their experiments, the reported surface energy for all grades of substrates were similar and within the error of the experimental measurements.

Interfacial Surface Adhesion Reduction. In the current study, we report changes of the substrate pull-off forces and thereby its surface energy by more than five times, with strong correlation with the number of F atoms per oligomer (Table 2). We also observed a modest reduction (~15%) of the surface modulus and modest changes of the contact angle and the corresponding surface energy (Table 1), though we observed strong changes (nearly an order of magnitude) in the mean asperity RMS roughness of the examined surfaces (Table 3). Apparently, the synergistic effect of these three factors have resulted in more than a five-fold reduction of the interfacial adhesion force. To understand such synergistic effect, the major interaction forces between the lunar dust simulant and the substrate must be considered. The two major interacting forces are those arising from the electrostatic and van der Waals (VDW) interactions. The electrostatic forces were estimated to be on the order of 1 nN for smooth or irregular shaped particles (Hays 1995, 1996). The simplified models of electrostatic attraction between the particle and the substrate account for a very small fraction of the adhesion forces. Thus, it can be safely argued that the VDW interactions have the strongest influence on the adhesion forces in the current framework, while the electrostatic forces have a very weak influence.

The VDW force can be estimated from Hamaker theory for an idealized spherical particle on a planar substrate (Hamaker, 1937) or according to contact mechanics theories (e.g. DMT and JKR). The interaction VDW force is given by,

$$F_A = \frac{H R_p}{6 s_o^2} \tag{7}$$

where, H is the Hamaker constant (~10^{-19} J in air), s_o is distance of closest approach between surfaces (~ 0.3 nm), and R_p is the particle radius. Noting that the adhesion force is the derivative of the potential energy with respect to the approach distance (Popov, 2010), the DMT and JKR theories can similarly provide the VDW forces as a function of the work of adhesion, w_s (in J/m^2),

$$F_A = 2\xi\pi R_p w_s \quad ; \quad \begin{cases} \xi = 1 & \text{for DMT} \\ \xi = \frac{3}{4} & \text{for JKR} \end{cases} \tag{8}$$

The work of adhesion, w_s is related to the surface energy of the particle γ_p and the substrate γ_s and their interfacial energy γ_{sp} ($\sim \sqrt{\gamma_s \cdot \gamma_p}$),

$$w_s = \gamma_s + \gamma_p - \sqrt{\gamma_s \cdot \gamma_p} \tag{9}$$

From Eqs. (7) and (9), the Hamaker constant can be estimated for each of the treated surfaces,

$$H = 12\pi\xi s_o^2 w_s \tag{10}$$

Utilizing Table 1 for the measured contact angle, γ_s can be evaluated for each surface. Using $\gamma_p = 50.54 mJ$ as that for silicon dioxide (Kinloch, 1987); w_s can be estimated for each of the examined substrates. Table 4 summarizes the estimated surface adhesion, work of adhesion and Hamaker constant (using $\xi = 1$) for each of the examined surfaces. It is evident that while the surface energy showed strong modulation with the F atoms per oligomer, both w_s and H are almost constant for the entire set of surfaces. Utilizing either Eq. 7 or Eq. 9 to estimate VDW force, the result will be almost independent of

the F atoms per oligomer. Thus, it can be concluded that the substrate surface energy has a negligible role in affecting the substrate work of adhesion and the corresponding adhesion pull-off forces.

Table 4. Summary of the calculated surface energy, work of adhesion and Hamaker constant

	Surface Energy (mJ/m^2)	**Work of Adhesion (mJ/m^2)**	**Hamaker Constant ($J \times 10^{-19}$)**
PI Control	25	39.99	1.357
$PIAEF_{18}$	8.7	38.27	1.298
$PIAEF_{30}$	15.7	38.07	1.291
$PIAEF_{30B}$	15.1	38.01	1.290
$PIAEF_{40}$	13.4	37.92	1.286
$PIAEF_{60}$	17.5	38.30	1.299

To understand the role of surface roughness on the adhesion pull-off force, it is well documented that asperities several order of magnitude smaller than the particle dimeter can greatly reduce the adhesion force from its idealized perfectly smooth interaction (Fuller et al., 1975; Rabinovich, et al. 2000a, 2000b). Approximating the surface roughness with hemispheres, Rumpf (1990) included the effect of a single hemispherical surface asperity on the adhesion of larger particle. Rabinovich, et al. (2000a, 2000b) modified Rumpf's approach to include a non-centered hemispherical asperity at the contact, yielding a model for the generalized adhesion force that depends on the surface RMS roughness of the dominant asperity and their wavelength, λ. The roughness modulated VDW adhesion force becomes,

$$F_A = \frac{H R_p}{6 s_o^2}\left(\frac{1}{1+\frac{58 R_p RMS}{\lambda^2}}+\frac{1}{\left(1+\frac{1.82 RMS}{s_o}\right)^2}\right) \qquad (11)$$

In Eq. 11, the first term represents the asperity-particle interaction, and the second term is the attraction forces from the rest of the surface and the particle, and tends to greatly diminish with increasing roughness. We utilized Eq. 10 to rationalize the role of the surface roughness, reported in Table 3 on the adhesion forces. Figure 11 summarizes the prediction of Eq. 11 for the adhesion forces

and compares it with the experimentally determined values. While the predicted force is lower than the measured values for the reference and low roughness surfaces, it over predicts the adhesion forces for the rougher surfaces. Qualitatively, this trend is similar to that reported trend by Rabinovich et al. (2000b), where increasing the roughness by an order of magnitude from 0.17 to 1.64 nm, decreased the adhesion forces by 3.7 times for a 10 μm glass sphere on a titanium surface. However, it is quite remarkable to reach an estimate of the adhesion forces that relies on two independent experimental measurements (contact angle and surface topology) and be of the same order of magnitude of the experimentally measured pull-off force from third independent measurements. The error of the predicted value of the adhesion force is within -10% of the experimentally measured value for the control sample, and within 35% for the highest F atoms per oligomer.

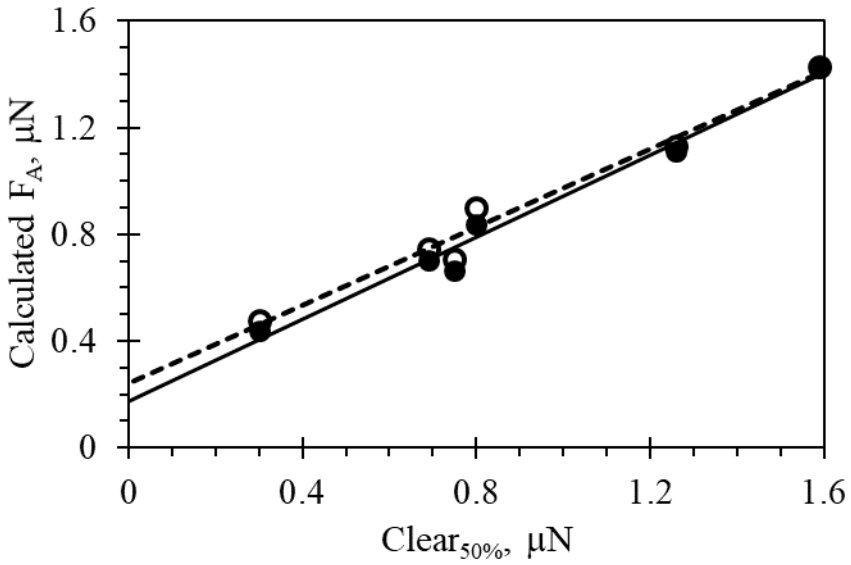

Figure 11. Comparison of experimentally determined adhesion force values, $Clear_{50\%}$, and adhesion force values calculated according to Eq. 11 (open symbols) and Eq. 13 (filled symbols). The dashed line and solid line are linear fits to values obtained from Eq. 11 and Eq. 13, respectively.

The remaining additional effect may stem from the mechanical properties of the substrate and their effects on modulating the pull-off adhesion force. To understand this effect, the dynamics of the experimental configuration should be considered, wherein the actuator forces are applied along the

particle pull-off direction. One might expect a larger effect of the kinematics of the substrate similar to the trampoline effect. During the forward stroke of the ultrasonic wand, the surface is pushing on the particle, with a force that reach its maximum at the end of the stroke. During this push-forward cycle, the substrate is being deformed underneath the contacting particle storing elastic strain energy. At the start of the reverse cycle, the substrate is almost elastically unloaded, and releasing this stored energy into the contact area. Then, the process dynamics are switched to pull-on forces on the particle. The kinematics of this process highlight the strong effect of the stored elastic strain energy within the substrate, and thereby the role of its elastic modulus. Realizing that the process dynamics of the sonic wand is a force control process, then an order of magnitude estimate from Hertzian contact can be utilized for a scaling purpose. The stored elastic strain energy within the substrate under a controlled applied load can be estimated from,

$$U_s \sim \frac{F_A^{5/3}}{E_r^{2/3} R_p^{1/3}} \tag{12}$$

It is evident that under the same applied particle indentation force on the substrate, the stored elastic strain energy within the substrate is increased for a more compliant substrate. This scaling can be utilized in a phenomenological way to either scale-up the measured adhesion force, or scale-down the predicted VDW forces by Eq. 11. For an order of magnitude analysis, we propose the scaling of VDW forces of Eq. 11,

$$F_A^* = \left(\frac{E_r\big|_{specimen}}{E_r\big|_{control}} \right)^{2/3} F_A \tag{13}$$

Equation 13 provides an approximate 10% reduction of F_A for a 15% reduction in the modulus, as highlighted in Figure 11. It is remarkable that the substrate modulus-modulation, while small appeared to be working in tandem with the surface roughness evolution to reduce the effective pull-off force and the work of adhesion of the copolyimide surfaces. Although not shown in Figure 11, the linear fit

generated from the values calculated from Eq. 13 had a slope closer to 1, a smaller y-axis intercept value, and a larger correlation coefficient, relative to the values calculated from Eq. 11, indicating better correlation with the experimental data.

Conclusions

Surface modifying agents have often been considered to play a limited role in changing surface properties, where only changes to surface chemical properties are considered. In the work described here, it has been demonstrated that their presence resulted in changes to surface chemical, topographical, and mechanical properties. These changes provided a synergistic effect toward reducing the adhesion interaction with lunar simulant particles. Utilization of these interaction-modifying surface properties in other material systems could lead to further development in lunar dust adhesion resistant materials. Decoupling the measurement technique influence, i.e., sonic wand motion imparting stored elastic strain energy in the substrate, on the results was critical to elucidate these interactions.

Acknowledgements

This work was funded through the Center Innovation Fund/Innovative Research and Development (CIF/IRAD) program at the NASA Langley Research Center. Ashraf Bastawros would also like to acknowledge the NASA Grant and Cooperative Agreement # NNX16AN21A, NNX16AL88H and work performed at Iowa State University.

References

Abbas, M. M., Tankosic, D., Craven, P. D., Spann, J. F., LeClair, A., West, E. A. 2007. “Lunar dust charging by photoelectric emissions.” *Planetary and Space Science*, 55(7-8), 953-965.

Afshar-Mohajer, N., Wu, C. Y., Curtis, J. S., Gaier, J. R. 2015. "Review of dust transport and mitigation technologies in lunar and Martian atmospheres." *Advances in Space Research*, 56, 1222-1241.

Banks, B. A., deGroh, K. K., Miller, S. K. 2004. *Low Earth Orbit Atomic Oxygen Interactions with Spacecraft Materials*, National Aeronautics and Space Administration, NASA TM-213400.

Barthlott, W., Neinhuis, C. 1997. "Purity of the sacred lotus, or escape from contamination in biological surfaces." *Planta*, 202, 1-8.

Bosse, T., Kleiser, L. 2006. "Small particles in homogenous turbulence: settling velocity enhancement by two-way coupling." *Physics of Fluids*, 18, 027102.

Calle, C. I., Mazumder, M. K., Immer, C. D., Buhler, C. R., Clements, J. S., Lundeen, P., Chen, A., Mantovani, J G. 2008. "Controlled particle removal from surfaces by electrodynamic methods for terrestrial, lunar, and Martian environmental conditions." *Journal of Physics: Conference Series*, 142, 012073.

Calle, C. I. 2017. Electrostatic phenomena on planetary surfaces. Morgan & Claypool Publishers.

Carr, M. H., Head, J. W. 2015. "Martian surface/near-surface water inventory: sources, sinks, and changes with time." *Geophysical Research Letters*, 42(3), 726-732.

Celia, E., Darmanin, T., de Givenchy, E. T., Amigoni, S., Guittard, F. 2013. "Recent advances in designing superhydrophobic surfaces." *Journal of Colloid and Interface Science*, 402, 1-18.

Chancellor, J. C., Blue, R. S., Cengel, K. A., Aunon-Chancellor, S. M., Rubins, K. H., Katzgraber, H. G., Kennedy, A. R. 2018. "Limitations in predicting the space radiation health risk for exploration astronauts". *npj Microgravity,* 4, 8.

Connell, J. W. 2000. "The Effect of Low Earth Orbit Atomic Oxygen Exposure on Phenylphosphine Oxide-Containing Polymers." *High Performance Polymers*, *12*(1), 43–52.

Dejesus C. M., Rimai, D. S. 2006. "Effect of Young's modulus on the detachment force of 7 μm particles." Hays, D. A. 1995. Fundamentals of Adhesion and Interfaces. Rimai, D. S., DeMejo, L. P., Mittal, K. L., Eds., VSP: Utrecht, The Netherlands, pp 61-71.

Derjaguin, B. V., Muller, V. M., Toporov, Y. P. 1975. "Effect of contact deformations on the adhesion of particles." *Journal of Colloid and Interface Science*, 53, 314–326.

Doerner M. F., Nix W. D. 1986. "Interpreting the data from depth-sensing indentation instruments." *Journal of Materials Research*, 1(4), 601-609.

Evans A. G., Hutchinson J. W. 1989. "Effects of non-planarity on the mixed mode fracture resistance of bimaterial interfaces." *Acta Metallurgica*, 37(3), 909-916.

Fuller, K. N. G., Tabor, D. 1975. "The effect of surface roughness on the adhesion of elastic solids." *Proceedings of the Royal Society A: Mathematical, Physical and Engineering Sciences*, 345, 327–342.

Gaier, J. R. 2005. *The effects of lunar dust on EVA systems during the Apollo missions.* National Aeronautics and Space Administration, NASA TM-213610.

Gaier, J. R.; Siamidis, J., Larkin, E. M. G. 2010. "Effect of Simulated Luanr Dust on the Properties of Thermal Control Surfaces." *Journal of Spacecraft and Rockets*, 47(1), 147-152.

Geim, A., Dubonos, S., Grigorieva, I. Novoselov, K. S., Zhukov, A. A., Shapoval, S. Y. 2003. "Microfabricated adhesive mimicking gecko foot-hair." *Nature Materials*, 2, 461–463.

Glaris, P., Coulon, J. F., Dorget, M., Poncin-Epaillard, F. 2015. "Surface migration of fluorinated additive during the curing of epoxy resin." *Composites Part B: Engineering*, 73, 10-15.

Goswami, N., Roma, P. G., De Boever, P., Clement, G., HArgens, A. R., Loeppky, J. A., Evans, J. M., Stein, T. P., Blaber, A. P., Van Loon, J. J. W. A., Mano, T., Iwase, S., Reitz, G., Hinghofer-Szalkay, H. G. 2012. "Using the Moon as a high-fidelity analogue environment to study the biological and behavioral effects of long-duration space exploration." *Planetary and Space Science*, 74(1), 111-120.

Grun, E., Horanyi, M., Sternovsky, Z. 2011. "The lunar dust environment." *Planetary and Space Science*, 59(14), 1672-1680.

Hamaker, H. C. 1937. "The London—van der Waals attraction between spherical particles." *Physica*, 4(10), 1058–1072.

Harney, M. B., Pant, R. R., Fulmer, P. A., Wynne, J. H. 2009. "Surface self-concentrating Amphiphilic quaternary ammonium biocides as coating additives." *ACS Applied Materials & Interfaces*, 1(1), 39-41.

Hays, D. A. 1996. Advances in Particle Adhesion; Rimai, D. S., Sharpe, L. H., Eds., Gordon and Breach: Amsterdam, pp 41-48.

Heiken, G. H., Vaniman, D. T., French, B. M. 1991. Lunar sourcebook, a user's guide to the Moon. Cambridge University Press.

Horányi, M., Szalay, J., Kempf, S., Schmidt, J., Grun, E., Srama, R., Sternovsky, Z. 2015. "A permanent, asymmetric dust cloud around the Moon." *Nature,* 522, 324–326.

Horenstein, M. N., Mazumder, M., Sumner Jr., R. C. 2013. "Predicting particle trajectories on an electrodynamic screen- theory and experiment." *Journal of Electrostatics*, 71(3), 1885-188.

International Space Exploration Coordination Group (ISECG). 2013. *Global Exploration Roadmap*, 2013, August 20. Posted at https://www.nasa.gov/sites/default/files/files/GER-2013_Small.pdf.

Johnson, K. L., Kendall, K., Roberts, A. D. 1971. "Surface energy and the contact of elastic solids." *Proceedings of the Royal Society, London Series A*, 324, 301–313.

Jung, Y. C., Bhushan, B. 2011. "Natural and biomimetic artificial surfaces for superhydrophocity, self-cleaning, low adhesion, and drag reduction." *Progress in Materials Science*, 56(1), 1-108.

Kinloch A. J. 1987. Adhesion and Adhesives. New York: Chapman and Hall, pp. 25.

Li, S., Lucey, P. G., Milliken, R. E., Hayne, P. O., Fisher, E., Williams, J. P., Hurley, D. M., Elphic, R. C. 2018. "Direct evidence of surface exposed water ice in the lunar polar regions." *Proceedings of the National Academy of Sciences*, 115 (36) 8907-8912.

Lim, S., Anand, M. 2019. "Numerical modelling of the microwave heating behavior of lunar regolith." *Planetary and Space Science*, 179, 104723.

Lim, S., Prabhu, V. L., Anand, M., Taylor, L. A. 2017. "Extra-terrestrial construction processes-advancements, opportunities and challenges." Advances in Space Research, 60(7), 1413-1429.

Liu, K., Jiang, L. 2012. "Bio-inspired and self-cleaning surfaces." *Annual Review of Materials Research*, 42(1), 231-263.

Liu, Y., Guan, Y., Zhang, Y., Rossman, G. R., Eiler, J. M., Taylor, L. A. 2012. "Direct measurement of hydroxyl in the lunar regolith and the origin of lunar surface water." *Nature Geoscience*, 5, 779–782.

Lorenz, R. D., Reiss, D. 2015. “Solar panel clearing events, dust devil tracks, and in-situ vortex detections on Mars.” *Icarus*, 248(1), 162-164.

Mckay, D. S., Cooper, B. L., Taylor, L. A., James, J. T., Thomas-Keprta, K., Pieters, C. M., Wentworth, S. J., Wallace, W. T., Lee, T.S. 2014. “Physicochemical properties of respirable-size lunar dust.” *Acta Astronautica*, 107, 163-176.

Murphy Jr., T. W., Adelberger, E. G., Battat, J. B. R., Hoyle, C. D., McMillan, R. J., Michelsen, E. L., Samad. R. L., Stubbs, C. W., Swanson, H. E. 2010. “Long-term degradation of optical devices on the Moon.” *Icarus*, 208(1), 31-35.

Nishimoto, S., Bhushan, B. 2013. “Bioinspired self-cleaning surfaces with superhydobrophobicity, superoleophobicity, and superhydrophilicity.” *RSC Advances*, 3, 671-690.

Nosonovsky, M., Bhushan, B. 2007. “Hierarchical roughness optimization for biomimetic superhydrophobic surfaces.” *Ultramicroscopy*, 107(10-11), 969-979.

Oliver W. C., Pharr G. M. 1992. “An improved technique for determining hardness and elastic modulus using load and displacement sensing indentation experiments.” *Journal of Materials Research*, 7(6), 1564-1583.

Oudayer, P., Mateo-Velez, J. C., Puybras, C., Roussel, J. F., Hess, S., Sarrailh, P., Murat, G. 2018. “Development of a new test bench dedicated to adhesion characterization of lunar dust simulants in space environment.” International Symposium on Materials in Space Environment (ISMSE 2018), Oct 2018, Biarritz, France. hal-02018290.

Pinson, J., Thiry, D. Eds. 2019. Surface modification of polymers: methods and applications. Wiley-VCH.

Popel, S. I., Golub, A. P., Zakharov, A. V., Zelenyi, L. M. 2020. “Formation of microspherules of lunar regolith in plasma-dust processes initiated by meteoroid impacts.” *Plasma Physics Reports*, 46(3), 219-226.

Popel, S. I., Zelenyi, L. M., Golub, A. P., Dubinskii, A. Yu. 2018. “Lunar dust and dusty plasmas: recent development, advances, and unresolved problems.” *Planetary and Space Science*, 156, 71-84.

Popov V. L. 2010. Contact mechanics and friction; physical principles and applications. Springer.

Quéré, D. 2008. “Wetting and Roughness.” *Annual Review of Materials Research*, 38(1), 71-99.

Rabinovich, Y. I., Adler, J. J., Ata, A., Singh, R. K., Moudgil, B. M. 2000a. “Adhesion between nanoscale rough surfaces I. Role of asperity geometry.” *Journal of Colloid and Interface Science*, 232, 10–16.

Rabinovich, Y. I., Adler, J. J., Ata, A., Singh, R. K., Moudgil, B. M. 2000b. “Adhesion between nanoscale rough surfaces: II. Measurement and comparison with theory.” *Journal of Colloid and Interface Science*, 232, 17–24. http://dx.doi.org/10.1006/jcis.2000.7168.

Rumpf, H. 1990. Particle technology. London/New York: Chapman & Hall.

Sangermano, M., Bongiovanni, R., Malucelli, G., Priola, A., Pollicino, A., Recca, A. 2003. “Fluorinated epoxides as surface modifying agents of UV-curable systems.” *Journal of Applied Polymer Science*, 89(6), 1524-1529.

Simonsen, L. C., Wilson, J. W., Kim, M. H., Cucinotta, F. A. 2000. "Radiation Exposure For Human Mars Exploration." *Health Physics: The Radiation Safety Journal,* 79(5), 515-525.

Stubbs, T. J., Vondrak, R. R., Farrell, W. M. 2006. "A dynamic fountain model for lunar dust." *Advances in Space Research*, 37(1), 59-66.

Tan, H., Xie, X., Li, J., Zhong, Y., Fu, Q. 2004. "Synthesis and surface mobility of segmented polyurethanes with fluorinated side chains attached to hard blocks." *Polymer*, 45(5), 1495-1502.

Thibeault, S., Kang, J., Sauti, G., Park, C., Fay, C., King, G. 2015. "Nanomaterials for radiation shielding." *MRS Bulletin*, 40(10), 836-841.

Walton, O. R. 2007. *Adhesion of lunar dust*. National Aeronautics and Space Administration, NASA CR-214685, prepared under contract NNC06VC87P.

Wang, H.-C. 1990. "Effects of inceptive motion on particle detachment from surfaces." *Aerosol Science and Technology*, 13, 386–393.

Wohl, C. J., Atkins, B. M., Connell, J. W. 2011. *Method and apparatus for the quantification of particulate adhesion forces on various substrates.* National Aeronautics and Space Administration, NASA TM-217048.

Wohl, C. J., Foster, L. L., Applin, S. I., Connell, J. W. 2015. "Synthesis and surface characterization of copoly(imide alkyl ether)s containing pendant fluoroalkyl groups." *Journal of Applied Polymer Science*, 132(9), 41538.

Wong, T., Kang, S., Tang, S., Smythe, E. J., Hatton, B. D., GRinthal, A., Aizenberg, J. 2011. "Bioinspired self-repairing slippery surfaces with pressure-stable omniphobicity." *Nature* **477,** 443–447.

Yang C., Lo C. T., Bastawros A. F., Narasimhan B. 2009. "Measurements of diffusion thickness at polymer interfaces by nanoindentation: A numerically calibrated experimental approach." *Journal of Materials Research*, 24(3), 985-992.

Yavas D., Bastawros A. F. 2017a. "Prediction of interfacial surface energy and effective fracture energy from contaminant concentration in polymer-based interfaces." *Journal of Applied Mechanics*, 84(4), 044501.

Yavas D., Shang X., Hong W., Bastawros A. F. 2017b. "Utilization of nanoindentation to examine bond line integrity in adhesively bonded composite structures." *International Journal of Fracture*, 204, 101-112.

Zhang, Y., Lin, R., Shi, Y., Li, H., Liu, Y., Zhou, C. 2019. "Synthesis and surface migration of polydimethylsiloxane and perfluorinated polyether in modified waterborne polyurethane." *Polymer Bulletin*, 76, 5517–5535.

Zimon, A. 1969. Adhesion of dust and powder. Plenum Press.